Constructing an active and stable oxygen electrode surface for reversible protonic ceramic electrochemical cells

Kai Pei [a,1], Shunrui Luo [b,1], Fan He [a], Jordi Arbiol [b,c], Yangsen Xu [a], Feng Zhu [a], Yakun Wang [a], Yu Chen [a,d,*]

[a] School of Environment and Energy, South China University of Technology, Guangzhou 510006, China
[b] Catalan Institute of Nanoscience and Nanotechnology (ICN2), CSIC and BIST, Campus UAB, Bellaterra, 08193 Barcelona, Catalonia, Spain
[c] ICREA, Pg. Lluís Companys 23, Barcelona 08010 Catalonia, Spain
[d] Guangdong Provincial Key Laboratory of Atmospheric Environment and Pollution Control, South China University of Technology, Guangzhou Higher Education Mega Centre, Guangzhou 510006, China

ARTICLE INFO

ABSTRACT

The reversible protonic ceramic electrochemical cells (R-PCECs) can efficiently and cost-effectively store and convert energy at low-intermediate temperatures (400-700 $^{\circ}$C). Their widespread commercialization is mainly limited by the challenges of oxygen electrodes due to the slow oxygen reaction kinetics and poor durability. In this study, we first enhance the reaction activity and surface stability of a double-perovskite $PrBaCo_2O_{5+\delta}$ (PBC) oxygen electrode by employing a fluorite-based $Pr_{0.1}Ce_{0.9}O_{2+\delta}$ (PCO) catalyst coating. The PCO-coated PBC (PCO-PBC) oxygen electrode shows a much-reduced area-specific resistance of 0.096 Ωcm^2 and good performance on a fuel-electrode supported single cell at 650 $^{\circ}$C, displaying a typical peak power density of 1.21 Wcm^{-2} (in fuel cell mode) and a typical current density of 2.69 Acm^{-2} at 1.3 V (in electrolysis mode) with reasonable faradaic efficiencies and durability. PCO coating has significantly improved the surface exchange process, facilitated ion diffusion, and suppressed the Ba-segregation of PBC, as confirmed by the analyses of electrochemical performance and TEM.

1. Introduction

With the urgent demand for low-carbon emissions, green hydrogen production technology has attracted extensive attention recently [1]. Compared with the traditional hydrogen production from the reforming and/or cracking of hydrocarbons, water electrolysis can produce hydrogen with much fewer impurities, avoiding other pollutions and potentially achieving zero carbon emission [2]. Among the emerging technologies for water electrolysis, solid oxide electrochemical cells (SOEC) have demonstrated great potential for high conversion efficiency and power density, fuel diversity, safety, modular assembly, and zero pollution [3,4]. Particularly, as highly efficient storage and energy conversion devices, reversible protonic ceramic electrochemical cells (R-PCECs) have become one of the most promising technologies for electric power generation in a fuel cell (FC) mode, and hydrogen production from water electrolysis in electrolysis (EL) mode. Since steam is provided to the oxygen electrode side, further hydrogen purification

becomes much easier, and the risk of Ni oxidation by a high concentration of steam in the fuel electrode can be potentially avoided [5].

However, the poor durability of oxygen electrodes, most likely caused by the undesired reaction of oxygen electrodes and steam, greatly hinders the further application of R-PCECs, more so at lower temperatures [6]. Furthermore, the oxygen reduction reaction (ORR) and oxygen evolution reaction (OER) in FC and EL modes, respectively, become more kinetically sluggish and complex at lower temperatures [7]. The worse performance and durability of R-PCEC are mainly caused by the polarization resistance increase of the oxygen electrodes, which often suffer from undesired surface segregation and/or surface structural deterioration [8]. To address these issues, oxygen electrodes with good long-term durability at a low cost are urgently needed.

Developing from highly active but unstable barium cobalt oxides materials, A-site cation-ordered, such as $LnBaCo_2O_{5+\delta}$-based double perovskites (Ln= lanthanide) have demonstrated great electrochemical performance and remarkable electrocatalytic activity of ORR and OER

* Corresponding author at: School of Environment and Energy, South China University of Technology, Guangzhou 510006, China.
E-mail address: eschenyu@scut.edu.cn (Y. Chen).
[1] These authors contributed equally to this work.

[9], following the order of Pr > Gd > Nd > Sm > La > Y[10]. The activities and stabilities of the double perovskite, including lattice oxygen and OER, have been systematically investigated in the $PrBaCo_2O_{5+\delta}$ (PBC) family [11,12]. Recently, great efforts have been made to unravel the mechanism of water splitting and the development of electrocatalyst materials [13]. Especially, PBC oxygen electrodes show variable structures and properties when the elemental doping is tuned [14]. For instance, $PrBa_{0.8}Ca_{0.2}Co_2O_{5+\delta}$ with Ca doping demonstrated a low polarization resistance ($\sim$0.24 Ω cm^2 at 600 ^{o}C) and great stability in humidified air with water content as high as 50% [15]. Bi-functional $PrBa_{0.9}Co_{1.96}Nb_{0.04}O_{5+\delta}$ material exhibited impressive cell performance while maintaining excellent stability [16]. A double perovskite $PrBaCo_{1.6}Fe_{0.2}Nb_{0.2}O_{5+\delta}$ (PBCFN) backbone covered by $PrBaCo_{1.6}Fe_{0.2}Nb_{0.2-x}O_{5+\delta}$ (Nb-deficient PBCFN) nano-particles, also exhibited high activity and durability in both FC and EL modes [7]. However, the PBC perovskite oxide materials often suffer from surface segregation (such as the formation of Ba-enriched surface clusters) [17], further causing slow kinetics and poor stability under high concentrations of H_2O in the electrolysis mode [18].

Surface modification of oxygen electrodes is one of the most effective methods to improve electrochemical activity and stability [19]. For example, Pei et al. applied barium cobaltite coatings on $La_{0.6}Sr_{0.4}Co_{0.2}Fe_{0.8}O_{3+\delta}$ (LSCF), which displayed an improved performance and durability of the oxygen electrode in the environment of chromium pollution and high concentration of CO_2 [20–22]. Bi et al. infiltrated $Sm_{0.5}Sr_{0.5}CoO_{3-\delta}$ (SSC) and PBC nano-particles into the BZY skeletons at the oxygen electrode side, showing an excellent power density at low temperatures [23]. Li et al. infiltrated $Y_{0.25}Bi_{0.75}O_{1.5}$ (YSB) into LSCF to achieve a lower interfacial polarization resistance [24]. Chen et al. reported a dual-phase catalyst of $PrNi_{0.5}Mn_{0.5}O_3$ (PNM) perovskite conformal layer with exsoluted fluorite PrO_x particles, displaying a low R_p of 0.052 Ωcm^2 and remarkable fuel cell performance stability at 700 ^{o}C [25]. Niu et al. introduced a $Pr_{1-x}Ba_xCoO_{3-\delta}$ thin film with exsoluted perovskite $BaCoO_{3-\delta}$ nano-particles for LSCF oxygen electrodes of R-PCECs, which demonstrated superior electrochemical performance [26].

The oxygen electrode of R-PCECs is exposed to the air with a high steam concentration in the process of electrolyzing water to produce hydrogen. This situation requires the oxygen electrode catalyst to have good durability in a high concentration of steam. However, perovskite materials may suffer from a long-term degradation issue due to the possible interaction of cations with steam at high temperatures. Therefore, a relatively stable fluorite-based Ceria doped with praseodymium oxides (PCO) material is chosen as the surface coating to enhance the durability of R-PCECs. PCO with a fluorite structure has shown good catalytic performance because of the mixed ionic-electronic conductivity, well-described ionic/electronic transport properties, and stability over limits of temperature and oxygen partial pressure [27]. In this work, we report our finding in improving the activity and durability of an oxygen electrode $PrBaCo_2O_{5+\delta}$ (PBC), enabled by a PCO catalyst coating. The cell with PCO-PBC oxygen electrode demonstrated high oxygen reaction activity and excellent durability under wet air at 650 ^{o}C (typical R-PCECs operation conditions). PCO coating on the PBC surface can provide more reaction sites and prevent the segregation of Ba, which enhance the activity and durability of power generation and hydrogen production. When the PCO-PBC oxygen electrode is applied on a $Ni-BaZr_{0.1}Ce_{0.7}Y_{0.1}Yb_{0.1}O_{3-\delta}$ (Ni-BZCYYb)-supported single cell, the cell delivers high performance at 650 ^{o}C, e.g., a typical peak power density of 1.21 Wcm^{-2} in FC mode and a current density of 2.69 Acm^{-2} at 1.3 V in EL mode.

2. Experimental

2.1. Fabrication of symmetrical cells, PCO catalyst coatings, and single cells

To evaluate the effect of PCO catalyst coatings on the electrochemical performance of oxygen electrodes, we have fabricated symmetrical cells with a dense $BaZr_{0.1}Ce_{0.7}Y_{0.1}Yb_{0.1}O_{3-\delta}$ (BZCYYb) electrolyte and porous PBC oxygen electrodes (on the two sides of BZCYYb). PBC powders were synthesized by the solution combustion method. BZCYYb was fabricated via a solid-state method. To be more specific, $BaCO_3$, ZrO_2, CeO_2, Y_2O_3, and Yb_2O_3 (all purchased from Macklin) were mixed at a stoichiometric ratio. Then the raw materials were added to a ball mill tank with a certain amount of ethanol. After ball milling for 24 h and drying overnight, the preliminary powder was pressed into a slice at 10 MPa and calcined at 1100 ^{o}C for 12 h. The pressing and calcination procedures are repeated twice to obtain a pure perovskite phase. Dense BZCYYb pellets with a relative density of $\sim$98% were mixed with 1% of NiO powder purchased from H2-BANK, then prepared by the dry-pressing method, followed by firing at 1450 ^{o}C for 5 h. PBC oxygen electrode was prepared by screen printing a slurry onto both sides of the BZCYYb electrolyte pellets. The cathode slurry was made by mixing the PBC power and terpinol (with 5 wt% ethyl cellulose) with a ratio of 1:0.8. The cells were then co-fired at 950 ^{o}C for 2 h to form a porous oxygen electrode (with an area of 0.28 cm^2, a typical size for a cell in lab-scale) on the dense BZCYYb electrolyte.

Aqueous nitrate precursors for PCO were prepared by dissolving certain amounts of nitrates into distilled water. Then stoichiometric amounts of glycine and polyvinylpyrrolidone (PVP) were added to the solutions as a complexing agent and a surfactant. The PCO catalyst solution was then dropped on the PBC backbone using a micro-liter syringe and followed by firing at 800, 900, and 1000 ^{o}C in the air for 2 h. The catalyst loading is approximately 0.3 mg, 0.6 mg, and 0.9 mg per square centimeter deposited on the backbone. Electrochemical impedance spectroscopy (EIS), distribution of relaxation time (DRT), scanning electron microscopy (SEM), transmission electron microscopy (TEM), and X-ray photoelectron spectroscopy (XPS) were used to study the evolution of interfacial polarization resistance (R_p), morphology and structure of PBC and PCO-PBC.

The Ni-BZCYYb fuel electrode-supported half-cells were manufactured via a co-tape casting process. The electrolyte slurry, functional layer slurry, and Ni-BZCYYb fuel electrode slurry were successively cast onto the polymer film. 15 h of drying in ambient air were needed to make sure the tape was dry thoroughly. Then the green tape was punched into pellets (about 15 mm in diameter) and pre-heated at 600 ^{o}C for 2 h to obtain sufficient mechanical strength. An extremely slow heating rate of 0.5 ^{o}C per minute was applied to remove the organics in the tape slowly. Finally, the pre-heated pellets were calcinated at 1450 ^{o}C for 5 h to form fuel electrode-supported half cells. For the single cell, the PBC oxygen electrode was applied onto the electrolyte of half cells through a screen-printing method. The PBC screen-printing ink was prepared by mixing PBC powder and terpinol (with 5 wt% ethyl cellulose) with a ratio of 1:0.8 after the ground for one hour in an agate mortar. The anode-supported cells were then mounted on an alumina tube with the Ceramic bond 552.

2.2. Electrochemical testing

The X-ray diffraction (XRD) pattern was detected with the Bruker D8 advance (Germany Bruker) instrument under Cu Kα radiation (λ = 0.15406 nm). The SEM images were detected by scanning electron microscopy (SEM, Hitachi SU8010, Japan). The fuel cells' performance was evaluated by testing cells with 3% H_2O humidified hydrogen in the fuel electrode and ambient air in the oxygen electrode. The electrolysis cell performance was evaluated by testing cells with 3 vol% H_2O humidified hydrogen in the fuel electrode and 3 vol% H_2O humidified air

in the oxygen electrode. The humidity of 3 vol% is controlled by flowing the gas through a water-bubbler at room temperature (about 25 °C). For most of the tests, button cells with an effective area of 0.28 cm² were used.

For the FC mode test, the fuel electrode was exposed to 30 mL min⁻¹ humidified H₂ (3 vol% H₂O) and the oxygen electrode was exposed to ambient air. For the EL mode test, the fuel electrode was fed with 30 mL min⁻¹ humidified H₂ (3 vol% H₂O) and the oxygen electrode was exposed to 40 mL min⁻¹ humidified (3 vol% H₂O) air. The steam concentration was controlled by a humidification system (LC-100, HP Pump). Faradaic efficiencies (η_F) were measured based on the ratio of the experimental and theoretical hydrogen generation amounts at fixed current densities. 45 mL min⁻¹ 10 vol% H₂-90 vol% Ar was fed to the fuel electrode and 100 mL min⁻¹ humidified air was fed to the oxygen electrode. Gas chromatography was used to monitor the hydrogen concentration in the fuel electrode, which was used to calculate the amount of actual hydrogen generated. The silver wires were connected with the fuel electrode and oxygen electrode, respectively, with help of a silver paste to collect the current. The current density-voltage curves, as well as impedance spectra of single cells, were measured using an electrochemical potentiostat (PARSTAT MC 200) at temperatures of 600-700 °C.

3. Results and discussion

3.1. Electrochemical activity, chemical stability, phase structure, and morphology of PBC and PCO-PBC oxygen electrode

Shown in Fig. 1a is the typical ASR temperature dependence of the bare PBC and PCO-PBC oxygen electrode, by measuring the symmetrical cells in the configuration of electrode | electrolyte | electrode in wet air with 3 vol% H₂O at 650 °C. The relatively higher reaction activity of the PCO-PBC electrode (sintered at 900 °C with a mass loading of 0.6 mg cm⁻²) is likely due to the better cohesion or the cation diffusion between the two phases. Details of the performance and surface micromorphology of PCO-PBC electrodes under different conditions are shown in Figs. S1, S2, and S3 and summarized in Table S1. The R_p values of the PCO-PBC oxygen electrode are 0.037, 0.214, and 1.751 Ωcm² at 700, 600, and 500 °C, respectively, which are much lower than those of the bare PBC oxygen electrode (0.078, 0.507, and 3.996 Ωcm² at 700, 600, and 500 °C, respectively). Fig. 1b shows the short-term (100 h) durability of symmetrical cells (of bare PBC and PCO-PBC) at OCV conditions in wet air at 650 °C. R_p of bare PBC increased dramatically in the first 50 h and continue to increase afterward. While the R_p of PCO-PBC remained to be ~0.10 Ωcm², which suggests that PCO catalysts can enhance the durability of PBC oxygen electrodes in wet air. The optimization of the composition in PCO catalysts are based on the performance and stability evaluation of R_p, as shown in Fig. S4. During the short-term testing at 650 °C under flowing air with 3 vol% H₂O, the R_p of the CeO_{2-δ}-PBC oxygen electrode can be reduced to ~0.10 Ωcm² initially, but then
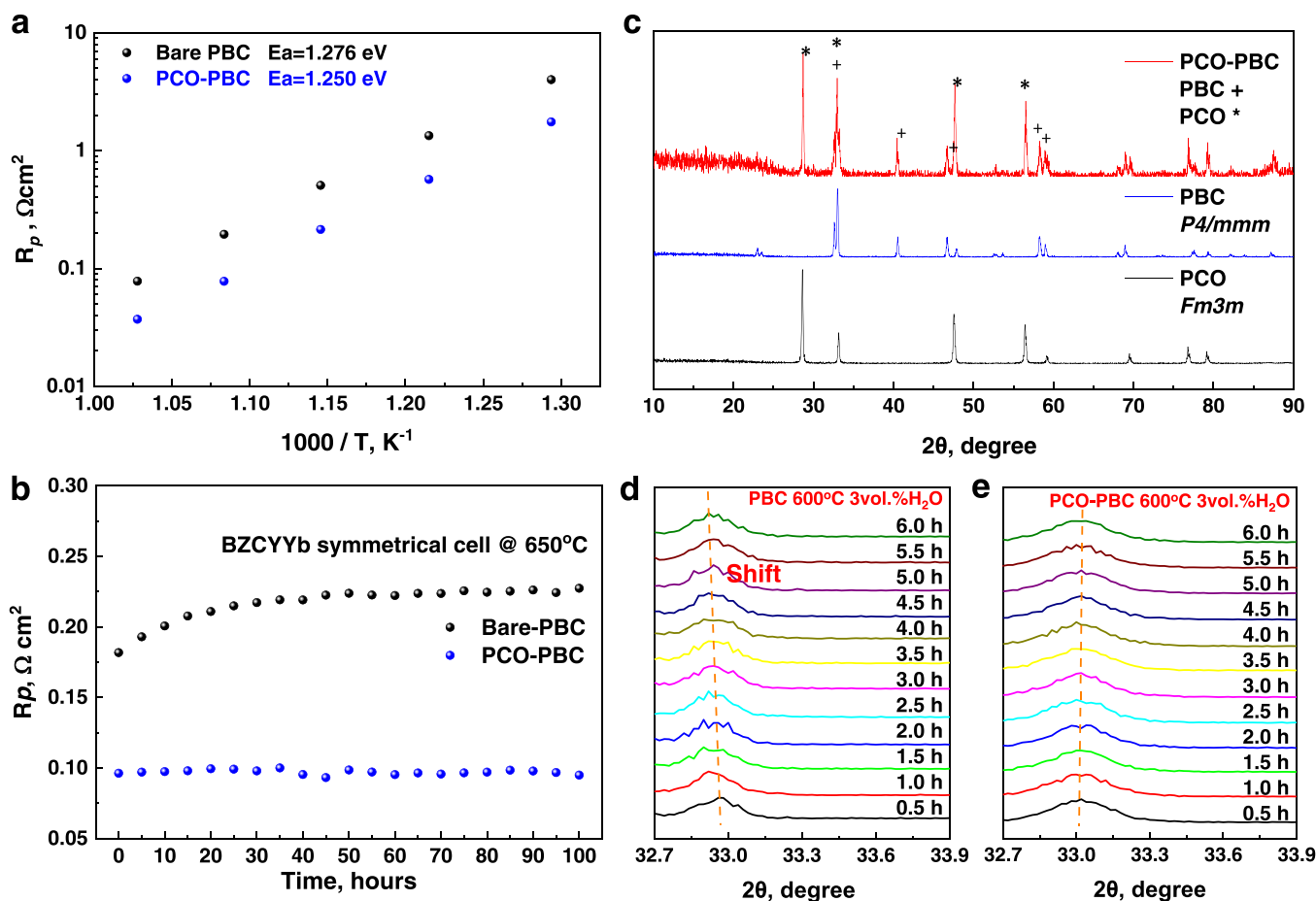

Fig. 1. (a) The ASR of a bare PBC electrode and a PCO-PBC electrode at a temperature range from 500 to 700 °C in wet air with 3 vol% H₂O; (b) The ASR stability test of a bare PBC electrode and a PCO-PBC electrode within 100 h at 650 °C; (c) XRD patterns of as-prepared PCO (black), PBC (blue), and mixed PCO-PBC (mass ratio of 1:1) powders (red) after calcining at 900 °C for 2 h in the air; *In situ* XRD patterns of PBC (d) and PCO-PBC (e) powders operated under wet air (3 vol% H₂O) at 600 °C for 6 h; the data were collected every 30 min.

increased to ~0.14 Ωcm^2 at 100 h. The $Pr_{0.2}Ce_{0.8}O_{2-\delta}$ catalyst can obtain ideal stability, however, the initial R_p of $Pr_{0.2}Ce_{0.8}O_{2-\delta}$-PBC increased to ~0.13 Ωcm^2.

Fig. 1c shows the XRD pattern of as-prepared PCO (black), PBC (blue), and mixed PCO-PBC powders (red) after being calcined at 900 °C for 2 h in the air. The mixed powder only shows the peaks from PCO and PBC, suggesting that no observable reactions occurred between PCO and PBC under typical operating conditions. The powder of PBC also showed good compatibility with BZCYYb electrolyte after being fired at 1000 °C (Fig. S5). *In situ* XRD examination of PBC was carried out in wet air at 600 °C, which indicates the steam-induced structure expansion (elongated metal-oxygen bonds) of the PBC electrode under high temperature (Fig. 1d and Fig. S6a), The slight structural change was likely caused by the lattice expansion during the exposure at 600 °C to wet air[28]. When interacting with water, parental PBC grains may have some surface elements segregation, as the main peak ($2\theta = 33°$) in XRD shifted as a function of time at 600 °C in wet air. However, the peak position of PCO-PBC can remain stable, suggesting that the lattice of PCO-PBC is not changing in steam, and surface enrichment may not be formed (Fig. 1e and Fig. S6b), while the catalyst suffered a significant morphological change, such as water absorption on the surface of ceria. In contrast, the composite electrode composed of PCO and PBC showed almost no lattice expansion, due likely to the fact that the PCO coating on the PBC surface would block the direct contact between water vapor and the PBC oxygen electrode. The water vapor may preferentially react with the Ce and inhibit the precipitation of Ba, thus maintaining the perovskite crystal structure of PBC.

Shown in Fig. 2 are the HAADF STEM images of PCO-PBC powder after being operated under wet air (3 vol% H_2O) at 600 °C for 100 h. The lattices in the red squared region (i) of Fig. 2 are assigned to the PCO phase. Details of the yellow squared region image from the PCO-PBC powder and the corresponding indexed power spectrum indicate that

Fig. 2-i nanoparticle has a crystal phase (space group of *Fm3m*) matching with the $Pr_{0.1}Ce_{0.9}O_2$ cubic phase with a=b=c= 5.4434 Å. From the selected crystalline domain (squared in orange) we obtain the corresponding power spectrum (fast Fourier transform (FFT)). The selected frequencies (spots) measured in the reciprocal space are equivalent to lattice fringe distances of 0.310 nm, 0.322 nm, and 0.275 nm, at 70.0° and 52.2°, which can be attributed to the (1−11), (1−1−1) and (002) planes of the cubic $Pr_{0.1}Ce_{0.9}O_2$ crystal phase, visualized along its [110] zone axis, as shown in Table S2. While the frequency spots measured in Fig. 2-ii power spectrum are corresponding to the (020), (11−2), and (10−2) planes of PBC, respectively. Indexed power spectrum and other corresponding details in the yellow squared region reveal that Fig. 2-ii selected nanoparticle has a crystal phase that could be in agreement with the $PrBaCo_2O_{5.49}$ tetragonal phase (space group = *P4/mmm*) with a=b= 3.9554 Å, c= 7.7070 Å. From the power spectrum obtained on the selected crystalline domain, the $PrBaCo_2O_{5.49}$ frequencies measured correspond to lattice fringe distances of 0.199 nm, 0.229 nm, and 0.277 nm, at 56.1° and 91.7° which could be interpreted as the cubic $PrBaCo_2O_{5.49}$ phase, visualized along its [201] zone axis, as shown in Table S3. HRTEM micrographs in Fig. 2 revealed that the shell covering the PBC grains is composed of PCO crystals. This is further confirmed by the high-angle annular dark-field (HAADF) STEM image of PCO-PBC powder with the corresponding X-ray energy dispersive spectrum (EDX) elemental analysis. Fig. 2 shows the EDX mapping for Ce, Pr, Ba, Co, and O elements, demonstrating that Ce is mainly found at the surface (shell) crystals. All these results demonstrate that the surface of PBC powder is covered by PCO grains. In contrast, the HRTEM image of PBC grains treated under 3 vol% H_2O at 650 °C after 100 h showed that $BaCO_3$ nanoparticles were segregated on the surface of PBC (PrBa$Co_2O_{5.82}$) nanocrystals. According to HRTEM analysis (Table S3), the presence of the PCO-PBC phase in our samples, which presents more oxygen vacancies than the PBC (PrBa$Co_2O_{5.82}$) crystal phase, indicates
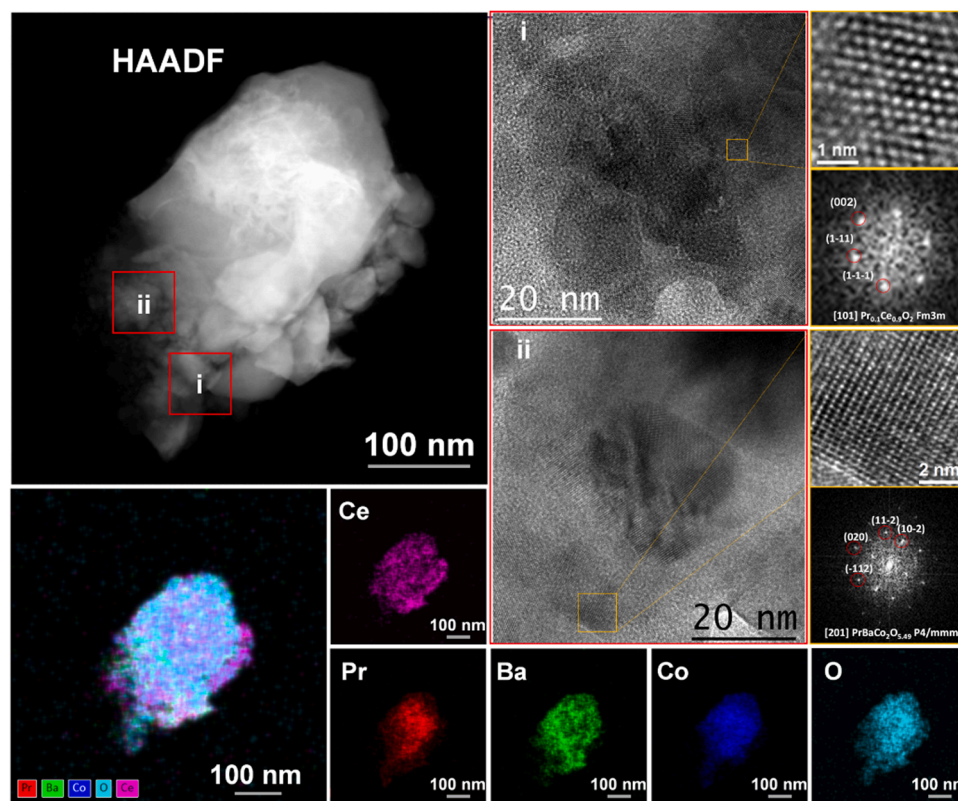

Fig. 2. High-angle annular dark-field (HAADF) STEM micrograph of PCO-PBC grains, including (i) PCO and (ii) PBC: details of the yellow squared regions, HRTEM image from the PCO and PBC powder and the corresponding power spectra indexation; and the X-ray energy dispersive spectrum mapping include Ce, Pr, Ba, Co, and O.

improved ORR performance of PCO-PBC.

3.2. Distribution of relaxation time (DRT) analyses

For understanding the details of the evolutions of detailed electrochemical processes on bare PBC and PCO-PBC under wet air conditions at 650 °C, the EIS of electrodes was analyzed carefully via the analyses of the distribution of relaxation time (DRT). The DRT plots (shown in Fig. 3a and 3b) and the EIS (shown in Fig. S7) of bare PBC and PCO-PBC were carefully tested and calculated under different oxygen partial pressure (p_{O2}).

The oxygen reduction/evolution reactions can be divided into different elementary reaction steps by Matlab calculation; the polarization resistance (R_p) that occurred on the oxygen electrode of each elementary reaction step can be attributed to the areas of DRT plots peaks. The R_p of each process is proportional to p_{O2}, following the equation of $R_p = k(p_{O2})^{-n}$. Fig. 3c and d show the function of different p_{O2} and the R_p in different frequency bands (marked as Low Frequency: green LF- P1, Intermediate Frequency: red IF- P2, and High Frequency: blue HF- P3) at 650 °C for bare PBC and PCO-PBC, respectively. The **n** value for LF- P1, IF- P2 and HF- P3 denoted near three color lines correspond to the different elementary reactions, shown in Table S6. As the details shown in Fig. 3c, the green line n_{LF} of bare PBC is 0.442, which is close to $3/8$). It means that P1 (LF) is corresponding to an oxygen dissociation process ($O_{ad} + e^- \rightarrow O_{ad}^-$), closely associated with the surface

exchange and ion diffusion process[29]. The red line n_{IF} of 1.184 (close to 1) may suggest that P2 (IF) is related to the gas diffusion process that occurred on the surface of bare PBC ($O_{2(g)} \rightarrow 2\ O_{ad}$)[30]. Shown in Fig. 3d are the DRT details of PCO-PBC under different p_{O2}. Similarly, the n_{LF} of PCO-PBC is 0.206, which indicates that green line P1 (LF) is likely corresponding to the oxygen dissociation that occurred in the interface between PCO and PBC ($O_{ad}^- \rightarrow O_{lattice}^-$,) and on the surface of PCO ($O_{ad} + e^- \rightarrow O_{ad}^-$ same with that of PBC). The impedance at LF of PCO-PBC is much lower than that of bare PBC. While the n_{IF} of P2 (IF) is 0.934, closely associated with the PCO-PBC oxygen electrode surface gas diffusion process ($O_{2(g)} \rightarrow 2\ O_{ad}$). The P1 and P2 processes of PCO-PBC include the corresponding processes of PBC bulk and PCO coating promotes the reaction rate on the oxygen electrode surface, thus promoting the reaction rate on the oxygen electrode surface. With the PCO on the PBC surface, the detailed reactions on the hetero-structured electrode may become complex. It is reasonable to see the different assignments; P1 and P2 in the two different materials may represent different processes. At the high-frequency range (around 10^4 Hz), both blue lines of bare PBC (0.087) and PCO-PBC (0.071) are close to zero, which is insensitive to p_{O2}, only the O^{2-} transfer across the electrode/electrolyte interface is related to this situation[31]. The rate-determining steps for both bare PBC and PCO-PBC oxygen electrodes were summarized in Table S7.

Shown in Fig. 3e and f are the comparison of DRT details with the bare PBC and PCO-PBC oxygen electrodes based on symmetrical cells,
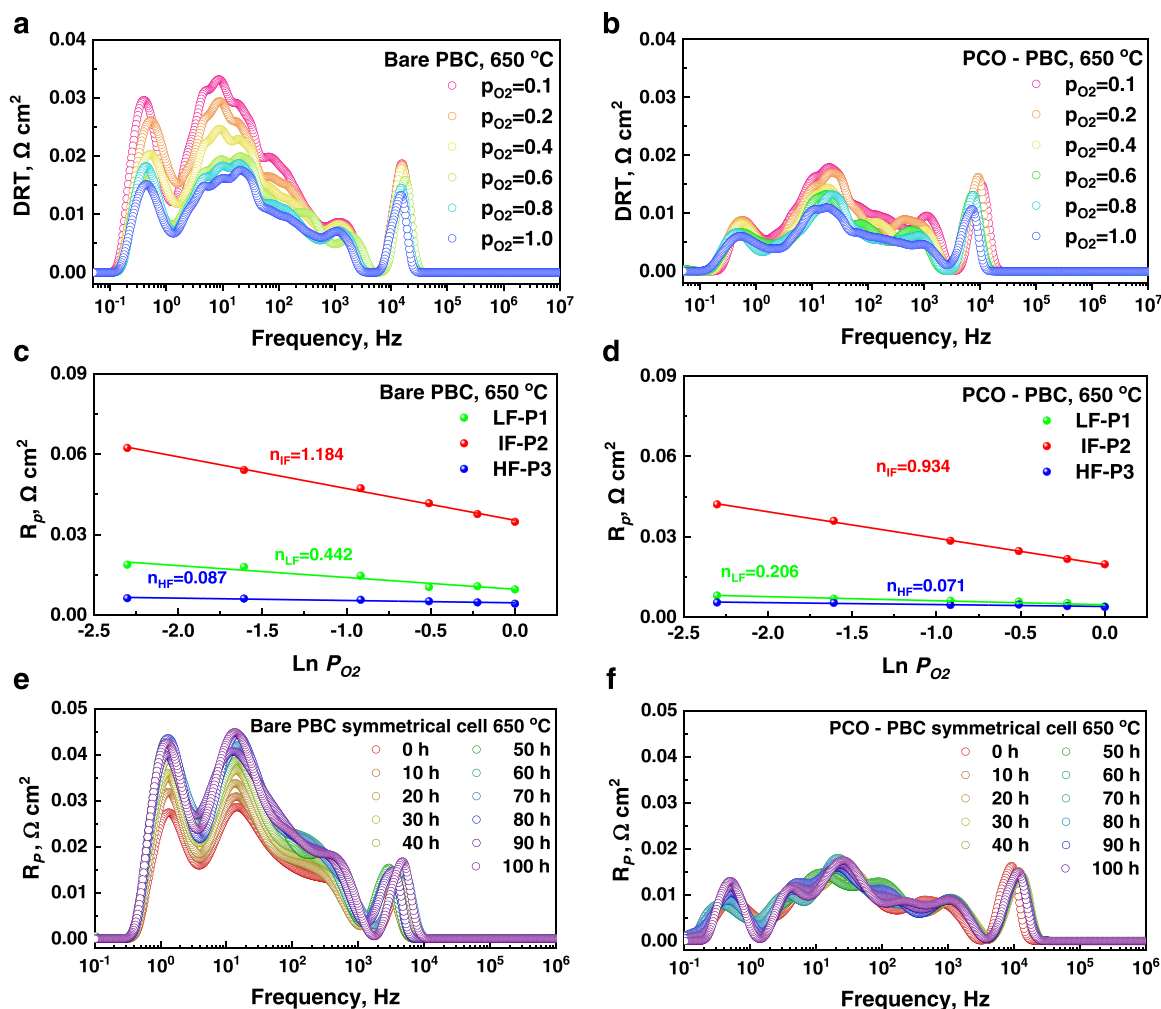

Fig. 3. Influences of oxygen partial pressure (p_{O2}) based on the DRT calculations of (a) Bare PBC and (b) PCO-PBC cathode evaluated at 650 °C; Dependence of p_{O2} on the resistance of each frequency range (Low Frequency: LF-P1, Intermediate Frequency: IF-P2, and High Frequency: HF–P3) for bare PBC(c) and PCO-PBC (d); Testing time evolution of the DRT curves of bare PBC (e) and PCO-PBC (f) at 650 °C under a flowing wet air with 3 vol% H_2O.

changing over the testing time in a flowing wet air with 3 vol% H_2O. It is clearly shown that the R_p of the bare PBC oxygen electrode in the LF (P1) (oxygen dissociation process) and IF (P2) (surface exchange and ion diffusion process) are the sources of the obvious increase of total R_p during the attenuation in humid air for a period of 100 h. The increased R_{LF} and R_{IF} should be attributed to the Ba particle segregation and coarsening issue, which block the active sites for surface oxygen reactions and limited the mass transfer process. While by surface modification of PCO, the areas of the P1 (LF) and the P2 (IF) are dramatically remain unchanged, indicating that both the surface exchange and ions diffusion) of PCO-PBC have been enhanced and stabilized.

The electrochemical behavior evolution of symmetrical cells was studied extensively under a different partial pressure of water (p$_{H2O}$) with 3 vol%, 10 vol%, 20 vol%, and 30 vol% H_2O steam at 650 °C for bare PBC and PCO-PBC, respectively, as shown in Fig. S8. With the increase in water pressure, the medium frequency (IF) impedance will increase. The PCO-PBC oxygen electrode can maintain stable performance under 30 vol% H_2O steam at 650 °C, while bare PBC can only maintain below 20 vol% H_2O steam at the same condition. Shown in Fig. S9 is the electrochemical performance (at 650 °C) of single cells with oxygen electrodes of bare PBC and PCO-PBC, respectively when the oxygen electrode is exposed to the air with 3 vol%, 10 vol%, 20 vol%, and 30 vol% H_2O steam. Single-cell with PCO-PBC oxygen electrodes showed good stability and high electrochemical performance even under 30 vol% H_2O steam content (as shown in Figs. S9b and S9d). However, a single cell with a PBC oxygen electrode showed a significant performance drop when tested in the air with 10 vol% and 20 vol% H_2O (as shown in Figs. S9a and S9c). Therefore, it may suggest that the PCO catalyst can protect the surface chemistry and structural stability of the PBC oxygen electrode under high concentrations of H_2O.
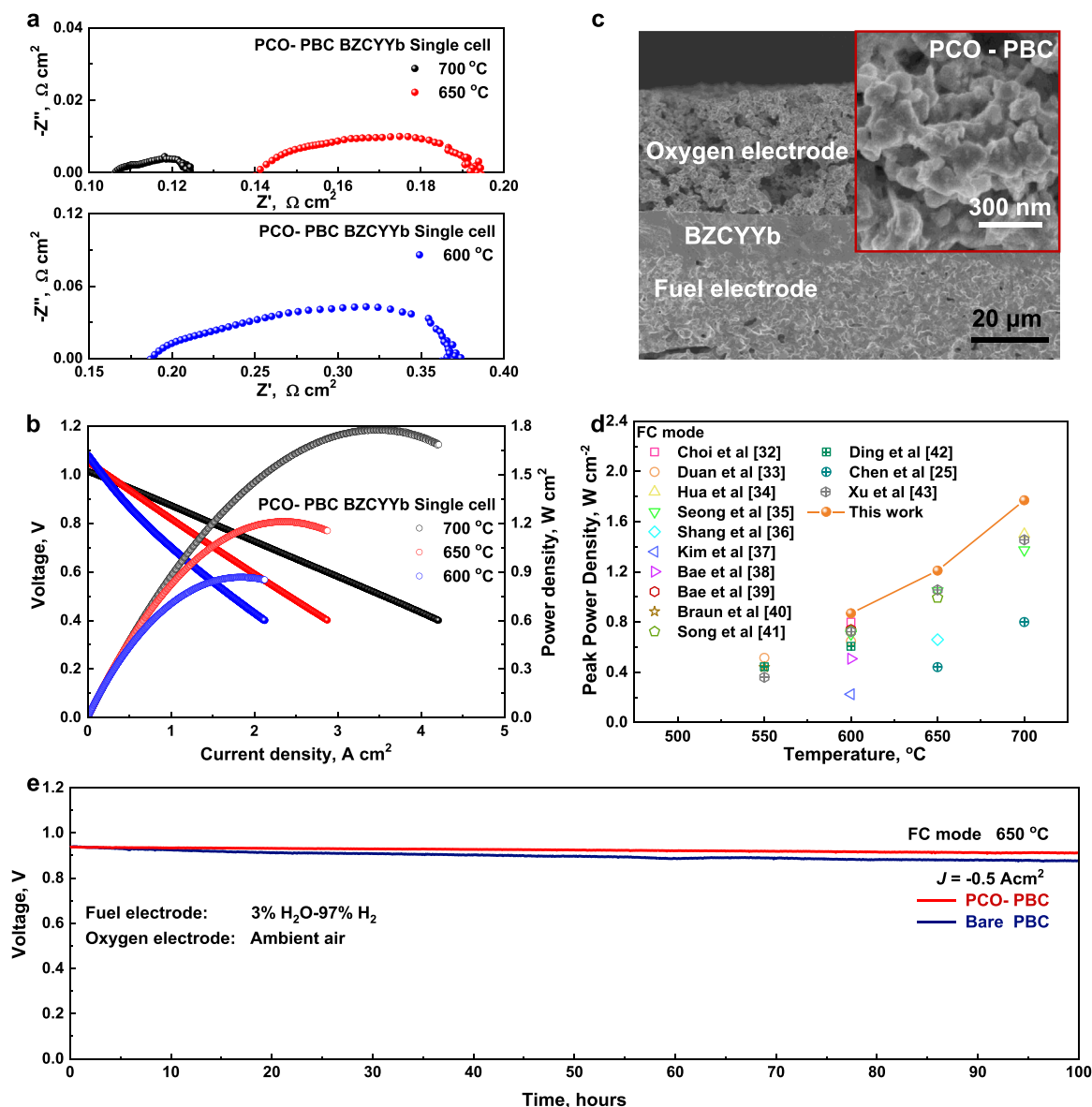

Fig. 4. The electrochemical performances of a fuel cell. (a) Typical EIS curves of the single-cell under OCV conditions with wet H_2 (3 vol% H_2O) as fuel and the ambient air as oxidant, measured at 700, 650, and 600 °C, respectively; (b) Typical cell current density-voltage-power (*I-V-P*) curves of the single-cell tested at 700 (black line), 650 (red line) and 600 (blue line) °C, respectively; (c) a cross-sectional SEM image of a single cell (Ni-BZCYYb fuel electrode supported) and the inserted SEM image of PBC oxygen electrode covered by PCO film; (d) comparison of the peak power densities of fuel cells with other materials reported, including PCO-PBC (this work); and (e) A short-term (100 h) stability evaluation of the PCO-PBC and PBC single-cell measures at the constant current density of 0.5 A cm^{-2} and 650 °C.

3.3. Electrochemical performances and surface morphology of a PCO-PBC oxygen electrode on a fuel cell

The electrochemical impedance spectra (EIS) curves of the single cell with PCO-PBC oxygen electrode were evaluated from 700 to 600 oC at open-circuit voltages as shown in Fig. 4a. The cell only showed a total resistance of 0.12 Ωcm^2, 0.19 Ωcm^2, and 0.36 Ωcm^2 at 700, 650, and 600 ^{o}C, respectively. Shown in Fig. 4b are the *I-V-P* curves of the PCO-PBC single-cell tested in the FC mode from 700 to 600 ^{o}C, under wet H_2 (3 vol% H_2O) worked as fuel and ambient air as oxidant. The single cell with the PCO-PBC oxygen electrode showed remarkable peak power densities (P_{max}) of 1.77, 1.21, and 0.87 W cm^{-2} at 700, 650, and 600 ^{o}C, respectively, which are much higher than that of bare PBC cell (1.57, 1.14, and 0.74 W cm^{-2} at 700, 650 and 600 ^{o}C, respectively, Fig. S10). A

cross-sectional SEM image of the single cell (Fig. 4c) displayed a porous PCO-PBC oxygen electrode layer with a thickness of 30 μm. The P_{max} of our cells surpasses most of the previous performance of the protonic ceramic fuel cells (shown in Table S8), as summarized in Fig. 4d[25, 32–43].

The cell with PCO-PBC oxygen electrode showed excellent stability during the FC mode at ($J= -0.5$ Acm^{-2}) testing, which retain 0.91 V output voltage at 650 ^{o}C after an operation of over 100 hrs, while the cell with bare PBC electrode dropped from 0.93 V to 0.87 V (shown in Fig. 4e). Performance evaluation (EIS and I-V-P curves) of the cells with bare PBC and PCO-PBC electrodes at initial and after 100 h of durability tests are shown in Fig. S11. In addition, PCO-PBC shows higher activity than bare PBC, which might be caused by the higher oxygen vacancy concentration of PCO-PBC than PBC alone[44,45], as confirmed by
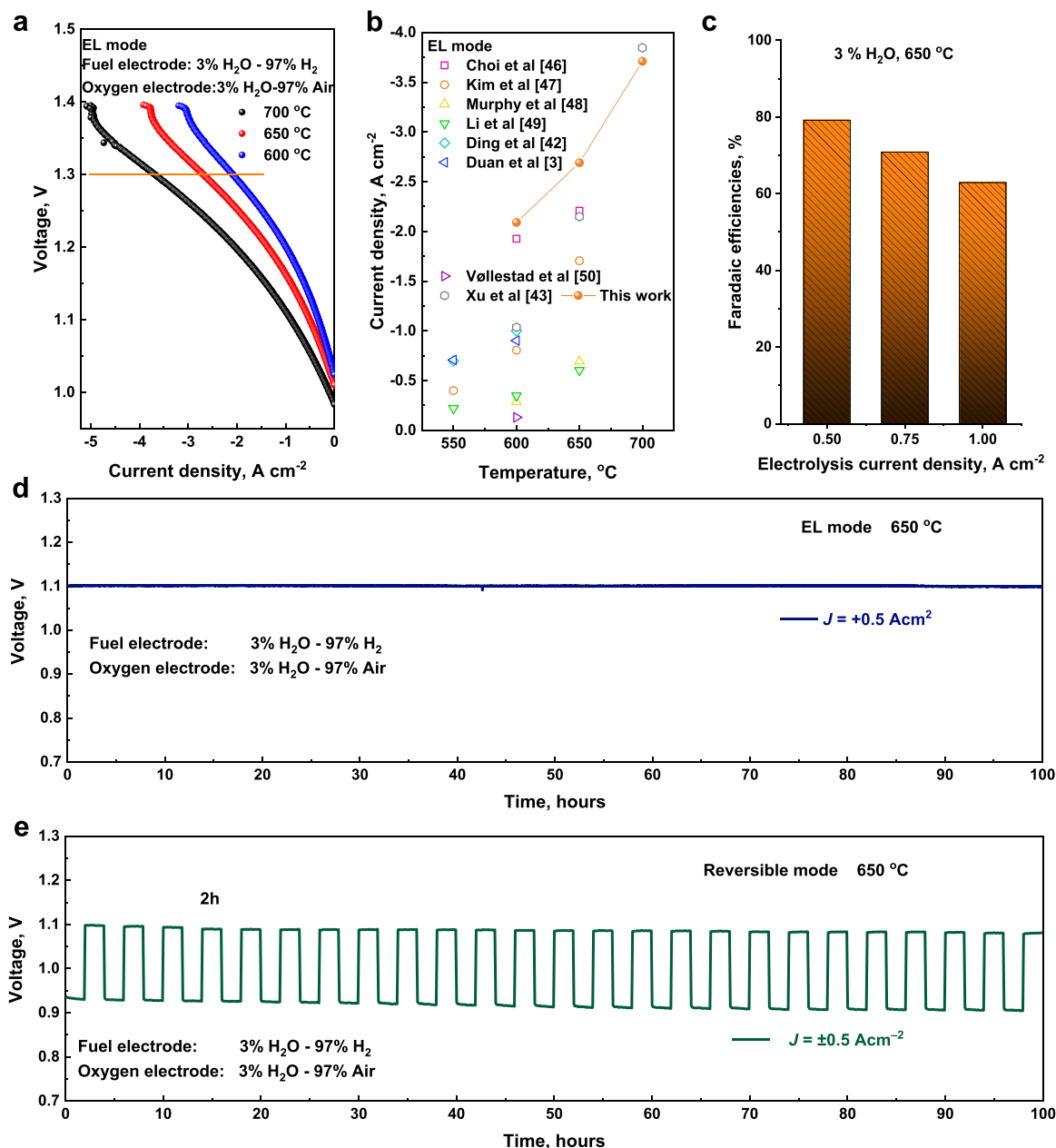

Fig. 5. Electrolysis performance. (a) Typical current-voltage (I-V) curves of the R-PCECs measured at 700, 650, and 600 ^{o}C, respectively with wet H_2 (3vol% H_2O) in the fuel electrode and wet air (3 vol% H_2O) in the oxygen electrode in EL mode; (b) Comparison of various oxygen electrode cobalt-based perovskite materials current densities, including PCO-PBC, tested at 1.3 V from 700 to 550 ^{o}C; (c) Faradaic efficiency of the cell at different electrolysis current densities; (d) Stability test of the single cell with PCO-PBC electrodes in EL mode (J=0.5 Acm^{-2}) at 650 ^{o}C; (e) Reversible operation at 650 ^{o}C of the PCO-PBC single-cell output voltage as a function of time by switching between the FC and EL modes under ± 0.5 Acm^{-2} current density for intervals of 2 h for each mode.

thermogravimetric analyses tested in the air from RT to 900 $^{\circ}$C, (with a ramping temperature of 10 $^{\circ}$C min^{-1}, shown in Fig. S12). The weight loss between 25 $^{\circ}$C to ~250 $^{\circ}$C may be assigned to the desorption of H_2O molecules[44,45]. The continuous weight loss after ~250 $^{\circ}$C was caused by the loss of lattice oxygen and the formation of oxygen vacancy[44, 45]. PCO-PBC is expected to possess a higher concentration of oxygen vacancy than PBC. The surface morphology changes of bare PBC and PCO-PBC before and after the test (~100 h) at 650 $^{\circ}$C in wet air were shown in Fig. S13. It is suggested that segregation behavior occurred on the surface of the PBC oxygen electrode after 100 h of testing in wet air at 650 $^{\circ}$C, which may indicate that Ba elements were precipitated from the electrode bulk (Fig. S13d).

It is noted that a Ba element segregation was observed in PBC after being operated under wet air (3 vol% H_2O) at 650 $^{\circ}$C for 100 h, compared with the relatively homogeneous Ba distribution in the initial PBC (Fig. S14). The segregated BaO would cover the active sites of PBC and result in a deterioration of ORR and OER performance. No obvious Ba element segregation was observed when PBC was decorated with a PCO coating (Fig. S15). The ratio of Co^{3+}/Co^{4+} in PCO-PBC (evaluated from the XPS spectrum) was kept stable after the operation in wet air (from 1.25 to 1.29), while the Co^{3+}/Co^{4+} ratio of PBC dropped from 1.68 to 0.92 after the operation (Fig. S16). A higher value of the Co^{3+}/Co^{4+} means that there are more oxygen vacancies in the oxygen electrode, likely suggesting a higher reaction activity, which is consistent with TEM results. Therefore, the PCO catalyst may keep the ORR/OER activity of the PCO-PBC oxygen electrode. Without the protection of PCO, PBC electrodes with $BaCO_3$ nanoparticles grown on the surface may have fewer oxygen vacancies (than PCO-PBC) under a water vapor environment, showing a significant degradation of electrochemical performance.

3.4. Electrochemical performance and Faradaic efficiency of PCECs with PCO-PBC oxygen electrodes

Moreover, the single cell with PCO-PBC oxygen electrode was also tested in EL and reversible mode. Shown in Fig. 5a are the typical current density–voltage (*I–V*) curves of the cell measured from 1.4 V to OCV (around 1 V) when the fuel electrode side was fed with wet hydrogen (3 vol% H_2O) and the oxygen electrode was exposed with a wet air (3 vol% H_2O). Promising current densities of ~3.71, 2.69, and 2.09 A cm^{-2} were achieved at 700, 650, and 600 $^{\circ}$C, respectively (1.3 V). A comparison of the current densities acquired from various oxygen electrodes from protonic ceramic electrolysis cells at a voltage of 1.3 V was shown in Fig. 5b and summarized in Table S9. It is confirmed that the performance of our cells is among the best, especially at 650 $^{\circ}$C [3,42,43,46–50]. The Faradaic efficiency of our cells is determined by calculating the ratio of the amount of H_2 detected to the theoretical H_2 amount. The air mixed with 3 vol% H_2O was injected at the oxygen electrode side to provide water. 10 vol% H_2/Ar was flowing at a speed of 10 mL min^{-1} into the fuel electrode side, using gas chromatography to test the exhaust gas discharged from the fuel electrode side. Displayed in Fig. 5c is the Faradaic efficiency measured at various electrolysis current densities at 650 $^{\circ}$C in 3 vol% H_2O for hydrogen production. It is shown that the Faradaic efficiency of cells at 0.5 A cm^{-2} is higher than those with an electrolysis current density of 0.75 Acm^{-2} and 1.00 Acm^{-2}, due likely to the electronic conduction of BZCYYb electrolytes at high current densities [51,52]. In addition, our cells showed relatively stable short-term durability (100 h) at 0.5 Acm^{-2} in EL mode at 650 $^{\circ}$C, as shown in Fig. 5d. Fig. S17 displays the current density-voltage (*I–V*) curves of the cell at the initial and after 100 h of the test, which are almost the same. PCO-PBC single cell could also maintain stability under different current densities of 0.50, 0.75, and 1.00 A cm^{-2} for 20 h (shown in Fig. S18). Moreover, a cycling test was operated, where the cell was running in dual modes of FC and EL. Fig. 5e demonstrates the cell voltages as a function of testing time when the operation mode was switched between the FC and EL modes (2 h for each mode) at 650 $^{\circ}$C

and $\pm$ 0.5 A cm^{-2}. The cell exhibited a slight degradation within 100 h and 25 cycles, demonstrating the high reversibility of the cells with the PCO-PBC oxygen electrode.

4. Conclusion

In summary, we constructed an active and durable catalyst coating on the surface of a perovskite-type oxygen electrode PBC by the infiltration of PCO for reversible protonic ceramic electrochemical cells. Single cells with PCO-coated PBC oxygen electrodes exhibited enhanced performances in both FC mode (e.g., a peak power density of 1.21 Wcm^{-2} at 650 $^{\circ}$C) and EL mode (e.g., a current density of 2.69 Acm^{-2} at 1.3 V for water electrolysis at 650 $^{\circ}$C). PCO catalyst-coated PBC oxygen electrode exhibit enhanced stability in wet air at 650 $^{\circ}$C, as confirmed by the high temperature *in situ* XRD analyses. PCO coating has significantly facilitated the surface exchange and diffusion, and suppressed the Ba-segregation of PBC, as confirmed by the analyses of electrochemical impedance spectra, distribution of relaxation time, and TEM. The demonstrated surface engineering design is highly attractive for R-PCECs and other types of energy conversion and storage devices, including solid-state batteries, supercapacitors, electrolytic water, electric reduction of carbon dioxide, and photocatalysis.

CRediT authorship contribution statement

Kai Pei: Investigation, Methodology, Data curation, Visualization, Writing – original draft. **Shunrui Luo:** Data curation, Methodology, Investigation, Writing – original draft. **Fan He:** Data curation, Investigation. **Jordi Arbiol**: Resources, Investigation, Methodology. **Yangsen Xu:** Data curation, Visualization. **Feng Zhu:** Data curation, Methodology. **Yakun Wang**: Methodology, Data curation. **Yu Chen:** Resources, Conceptualization, Supervision, Project administration, Writing – review & editing.

Declaration of Competing Interest

The authors declare that they have no known competing financial interests or personal relationships that could have appeared to influence the work reported in this paper.

Data Availability

Data will be made available on request.

by the CERCA Programme / Generalitat de Catalunya.

Appendix A. Supporting information

Supplementary data associated with this article can be found in the online version at doi:10.1016/j.apcatb.2023.122601.

References

[1] D. Chen, C. Chen, Z.M. Baiyee, Z. Shao, F. Ciucci, Nonstoichiometric oxides as low-cost and highly-efficient oxygen reduction/evolution catalysts for low-temperature electrochemical devices, Chem. Rev. 115 (2015) 9869–9921.

[2] Y. Zhou, E. Liu, Y. Chen, Y. Liu, L. Zhang, W. Zhang, Z. Luo, N. Kane, B. Zhao, L. Soule, Y. Niu, Y. Ding, H. Ding, D. Ding, M. Liu, An active and robust air electrode for reversible protonic ceramic electrochemical cells, ACS Energy Lett. 6 (2021) 1511–1520.

[3] C. Duan, R. Kee, H. Zhu, N. Sullivan, L. Zhu, L. Bian, D. Jennings, R. O'Hayre, Highly efficient reversible protonic ceramic electrochemical cells for power generation and fuel production, Nat. Energy 4 (2019) 230–240.

[4] Y. Chen, B. deGlee, Y. Tang, Z. Wang, B. Zhao, Y. Wei, L. Zhang, S. Yoo, K. Pei, J. H. Kim, Y. Ding, P. Hu, F.F. Tao, M. Liu, A robust fuel cell operated on nearly dry methane at 500 °C enabled by synergistic thermal catalysis and electrocatalysis, Nat. Energy 3 (2018) 1042–1050.

[5] K. Pei, Y. Zhou, K. Xu, H. Zhang, Y. Ding, B. Zhao, W. Yuan, K. Sasaki, Y. Choi, Y. Chen, M. Liu, Surface restructuring of a perovskite-type air electrode for reversible protonic ceramic electrochemical cells, Nat. Commun. 13 (2022) 2207.

[6] S. Kim, D.W. Joh, D.-Y. Lee, J. Lee, H.S. Kim, M.Z. Khan, J.E. Hong, S.-B. Lee, S. J. Park, R.-H. Song, M.T. Mehran, C.K. Rhee, T.-H. Lim, Microstructure tailoring of solid oxide electrolysis cell air electrode to boost performance and long-term durability, Chem. Eng. J. 410 (2021) 128318.

[7] Y. Zhou, W. Zhang, N. Kane, Z. Luo, K. Pei, K. Sasaki, Y. Choi, Y. Chen, D. Ding, M. Liu, An efficient bifunctional air electrode for reversible protonic ceramic electrochemical cells, Adv. Funct. Mater. 31 (2021) 2105386.

[8] Y. Niu, Y. Zhou, W. Lv, Y. Chen, Y. Zhang, W. Zhang, Z. Luo, N. Kane, Y. Ding, L. Soule, Y. Liu, W. He, M. Liu, Enhancing oxygen reduction activity and Cr tolerance of solid oxide fuel cell cathodes by a multiphase catalyst coating, Adv. Funct. Mater. 31 (2021) 2100034.

[9] E. Marelli, J. Gazquez, E. Poghosyan, E. Müller, D.J. Gawryluk, E. Pomjakushina, D. Sheptyakov, C. Piamonteze, D. Aegerter, T.J. Schmidt, M. Medarde, E. Fabbri, Correlation between oxygen vacancies and oxygen evolution reaction activity for a model electrode: PrBaCo2O5+δ, Angew. Chem. Int. Ed. 60 (2021) 14609–14619.

[10] K. Zhang, L. Ge, R. Ran, Z. Shao, S. Liu, Synthesis, characterization and evaluation of cation-ordered LnBaCo2O5+δ as materials of oxygen permeation membranes and cathodes of SOFCs, Acta Mater. 56 (2008) 4876–4889.

[11] A. Grimaud, K.J. May, C.E. Carlton, Y.L. Lee, M. Risch, W.T. Hong, J. Zhou, Y. Shao-Horn, Double perovskites as a family of highly active catalysts for oxygen evolution in alkaline solution, Nat. Commun. 4 (2013) 2439.

[12] B.-J. Kim, X. Cheng, D.F. Abbott, E. Fabbri, F. Bozza, T. Graule, I.E. Castelli, L. Wiles, N. Danilovic, K.E. Ayers, N. Marzari, T.J. Schmidt, Highly active nanoperovskite catalysts for oxygen evolution reaction: insights into activity and stability of Ba0.5Sr0.5Co0.8Fe0.2O2+δ and PrBaCo2O5+δ, Adv. Funct. Mater. 28 (2018) 1804355.

[13] E. Fabbri, A. Habereder, K. Waltar, R. Kötz, T.J. Schmidt, Developments and perspectives of oxide-based catalysts for the oxygen evolution reaction, Catal. Sci. Technol. 4 (2014) 3800–3821.

[14] J. Hwang, R.R. Rao, L. Giordano, Y. Katayama, Y. Yu, Y. Shao-Horn, Perovskites in catalysis and electrocatalysis, Science 358 (2017) 751–756.

[15] J.H. Kim, S. Yoo, R. Murphy, Y. Chen, Y. Ding, K. Pei, B. Zhao, G. Kim, Y.M. Choi, M. Liu, Promotion of oxygen reduction reaction on a double perovskite electrode by a water-induced surface modification, Energy Environ. Sci. 14 (2021) 1506–1516.

[16] W. Zhang, Y. Zhou, E. Liu, Y. Ding, Z. Luo, T. Li, N. Kane, B. Zhao, Y. Niu, Y. Liu, M. Liu, A highly efficient and durable air electrode for intermediate-temperature reversible solid oxide cells, Appl. Catal. B: Environ. 299 (2021), 120631.

[17] B. Wei, M. Schroeder, M. Martin, Surface cation segregation and chromium deposition on the double-perovskite oxide PrBaCo2O5+δ, ACS Appl. Mater. Interfaces 10 (2018) 8621–8629.

[18] W. Wang, D. Medvedev, Z. Shao, Gas humidification impact on the properties and performance of perovskite-type functional materials in proton-conducting solid oxide cells, Adv. Funct. Mater. 28 (2018) 1802592.

[19] D. Ding, X. Li, S.Y. Lai, K. Gerdes, M. Liu, Enhancing SOFC cathode performance by surface modification through infiltration, Energy Environ. Sci. 7 (2014) 552–575.

[20] K. Pei, Y. Zhou, K. Xu, Z. He, Y. Chen, W. Zhang, S. Yoo, B. Zhao, W. Yuan, M. Liu, Y. Chen, Enhanced Cr-tolerance of an SOFC cathode by an efficient electro-catalyst coating, Nano Energy 72 (2020), 104704.

[21] Y. Chen, Y. Choi, S. Yoo, Y. Ding, R. Yan, K. Pei, C. Qu, L. Zhang, I. Chang, B. Zhao, Y. Zhang, H. Chen, Y. Chen, C. Yang, B. deGlee, R. Murphy, J. Liu, M. Liu, A highly efficient multi-phase catalyst dramatically enhances the rate of oxygen reduction, Joule 2 (2018) 938–949.

[22] K. Pei, Y. Zhou, Y. Ding, K. Xu, H. Zhang, W. Yuan, K. Sasaki, Y. Choi, M. Liu, Y. Chen, An improved oxygen reduction reaction activity and CO2-tolerance of La0.6Sr0.4Co0.2Fe0.8O3-δ achieved by a surface modification with barium cobaltite coatings, J. Power Sources 514 (2021), 230573.

[23] L. Bi, S.P. Shafi, E.H. Da'as, E. Traversa, Tailoring the cathode–electrolyte interface with nanoparticles for boosting the solid oxide fuel cell performance of chemically stable proton-conducting electrolytes, Small 14 (2018) 1801231.

[24] G. Li, B. He, Y. Ling, J. Xu, L. Zhao, Highly active YSB infiltrated LSCF cathode for proton conducting solid oxide fuel cells, Int. J. Hydrog. Energy 40 (2015) 13576–13582.

[25] Y. Chen, S. Yoo, K. Pei, D. Chen, L. Zhang, B. deGlee, R. Murphy, B. Zhao, Y. Zhang, Y. Chen, M. Liu, An in situ formed, dual-phase cathode with a highly active catalyst coating for protonic ceramic fuel cells, Adv. Funct. Mater. 28 (2018) 1704907.

[26] Y. Niu, Y. Zhou, W. Zhang, Y. Zhang, C. Evans, Z. Luo, N. Kane, Y. Ding, Y. Chen, X. Guo, W. Lv, M. Liu, Highly active and durable air electrodes for reversible protonic ceramic electrochemical cells enabled by an efficient bifunctional catalyst, Adv. Energy Mater. 12 (2022) 2103783.

[27] D. Chen, S.R. Bishop, H.L. Tuller, Nonstoichiometry in oxide thin films operating under anodic conditions: a chemical capacitance study of the praseodymium–cerium oxide system, Chem. Mater. 26 (2014) 6622–6627.

[28] M. Irshad, R. Idrees, K. Siraj, I. Shakir, M. Rafique, Qu Ain, R. Raza, Electrochemical evaluation of mixed ionic electronic perovskite cathode LaNi1−xCoxO3-δ for IT-SOFC synthesized by high temperature decomposition, Int. J. Hydrog. Energy 46 (2021) 10448–10456.

[29] T. Matsui, N. Kunimoto, K. Manriki, K. Miyazaki, N. Kamiuchi, H. Muroyama, K. Eguchi, Oxygen reduction reaction over (Ba,Sr)6RE2Co4O15–Ba(Ce,Pr,Y)O3 composite cathodes for proton-conducting ceramic fuel cells, J. Mater. Chem. A 9 (2021) 15199–15206.

[30] D. Huan, L. Zhang, X. Li, Y. Xie, N. Shi, S. Xue, C. Xia, R. Peng, Y. Lu, A durable ruddlesden-popper cathode for protonic ceramic fuel cells, ChemSusChem 13 (2020) 4994–5003.

[31] F. He, M. Liang, W. Wang, R. Ran, G. Yang, W. Zhou, Z. Shao, High-performance proton-conducting fuel cell with B-site-deficient perovskites for all cell components, Energy Fuels 34 (2020) 11464–11471.

[32] S. Choi, C.J. Kucharczyk, Y. Liang, X. Zhang, I. Takeuchi, H.I. Ji, S.M. Haile, Exceptional power density and stability at intermediate temperatures in protonic ceramic fuel cells, Nat. Energy 3 (2018) 202–210.

[33] C. Duan, J. Tong, M. Shang, S. Nikodemski, M. Sanders, S. Ricote, A. Almansoori, R. O'Hayre, Readily processed protonic ceramic fuel cells with high performance at low temperatures, Science 349 (2015) 1321–1326.

[34] B. Hua, N. Yan, M. Li, Y.F. Sun, Y.Q. Zhang, J. Li, T. Etsell, P. Sarkar, J.L. Luo, Anode-engineered protonic ceramic fuel cell with excellent performance and fuel compatibility, Adv. Mater. 28 (2016) 8922–8926.

[35] A. Seong, J. Kim, J. Kim, S. Kim, S. Sengodan, J. Shin, G. Kim, Influence of cathode porosity on high performance protonic ceramic fuel cells with PrBa0.5Sr0.5Co1.5Fe0.5O5-δ cathode, J. Electrochem. Soc. 165 (2018) F1098–F1102.

[36] M. Shang, J. Tong, R. O'Hayre, A promising cathode for intermediate temperature protonic ceramic fuel cells: BaCo0.4Fe0.4Zr0.2O3−δ, RSC Adv. 3 (2013) 15769–15775.

[37] J. Kim, S. Sengodan, G. Kwon, D. Ding, J. Shin, M. Liu, G. Kim, Triple-conducting layered perovskites as cathode materials for proton-conducting solid oxide fuel cells, ChemSusChem 7 (2014) 2811–2815.

[38] K. Bae, H.S. Noh, D.Y. Jang, J. Hong, H. Kim, K.J. Yoon, J.H. Lee, B.K. Kim, J. H. Shim, J.W. Son, High-performance thin-film protonic ceramic fuel cells fabricated on anode supports with a non-proton-conducting ceramic matrix, J. Mater. Chem. A 4 (2016) 6395–6403.

[39] K. Bae, D.Y. Jang, H.J. Choi, D. Kim, J. Hong, B.K. Kim, J.H. Lee, J.W. Son, J. H. Shim, Demonstrating the potential of yttrium-doped barium zirconate electrolyte for high-performance fuel cells, Nat. Commun. 8 (2017) 14553.

[40] R.J. Braun, A. Dubois, K. Ferguson, C. Duan, C. Karakaya, R.J. Kee, H. Zhu, N. P. Sullivan, E. Tang, M. Pastula, A. Wood, T. Joia, R. O'Hayre, Development of kW-scale protonic ceramic fuel cells and systems, ECS Trans. 91 (2019) 997–1008.

[41] Y. Song, Y. Chen, W. Wang, C. Zhou, Y. Zhong, G. Yang, W. Zhou, M. Liu, Z. Shao, Self-assembled triple-conducting nanocomposite as a superior protonic ceramic fuel cell cathode, Joule 3 (2019) 2842–2853.

[42] H. Ding, W. Wu, C. Jiang, Y. Ding, W. Bian, B. Hu, P. Singh, C.J. Orme, L. Wang, Y. Zhang, D. Ding, Self-sustainable protonic ceramic electrochemical cells using a triple conducting electrode for hydrogen and power production, Nat. Commun. 11 (2020) 1907.

[43] K. Xu, H. Zhang, Y. Xu, F. He, Y. Zhou, Y. Pan, J. Ma, B. Zhao, W. Yuan, Y. Chen, M. Liu, An efficient steam-induced heterostructured air electrode for protonic ceramic electrochemical cells, Adv. Funct. Mater. (2022) 2110998.

[44] F. Dong, Y. Chen, D. Chen, Z. Shao, Surprisingly high activity for oxygen reduction reaction of selected oxides lacking long oxygen-ion diffusion paths at intermediate temperatures: a case study of cobalt-free BaFeO3-δ, ACS Appl. Mater. Interfaces 6 (2014) 11180–11189.

[45] W. Chen, T. Wen, H. Nie, R. Zheng, Study of Ln0.6Sr0.4Co0.8Mn0.2O3-δ (Ln⎯La, Gd, Sm or Nd) as the cathode materials for intermediate temperature SOFC, Mater. Res. Bull. 38 (2003) 1319–1328.

[46] S. Choi, T.C. Davenport, S.M. Haile, Protonic ceramic electrochemical cells for hydrogen production and electricity generation: exceptional reversibility, stability, and demonstrated faradaic efficiency, Energy Environ. Sci. 12 (2019) 206–215.

[47] J. Kim, A. Jun, O. Gwon, S. Yoo, M. Liu, J. Shin, T.H. Lim, G. Kim, Hybrid-solid oxide electrolysis cell: a new strategy for efficient hydrogen production, Nano Energy 44 (2018) 121–126.

[48] R. Murphy, Y. Zhou, L. Zhang, L. Soule, W. Zhang, Y. Chen, M. Liu, A new family of proton-conducting electrolytes for reversible solid oxide cells: BaHfxCe0.8−xY0.1Yb0.1O3−δ, Adv. Funct. Mater. 30 (2020) 2002265.

[49] W. Li, B. Guan, L. Ma, S. Hu, N. Zhang, X. Liu, High performing triple-conductive $Pr_2NiO_{4+\delta}$ anode for proton-conducting steam solid oxide electrolysis cell, J. Mater. Chem. A 6 (2018) 18057–18066.

[50] E. Vøllestad, R. Strandbakke, M. Tarach, D. Catalán-Martínez, M.L. Fontaine, D. Beeaff, D.R. Clark, J.M. Serra, T. Norby, Mixed proton and electron conducting double perovskite anodes for stable and efficient tubular proton ceramic electrolysers, Nat. Mater. 18 (2019) 752–759.

[51] T. Hu, F. He, M. Liu, Y. Chen, In situ/operando regulation of the reaction activities on hetero-structured electrodes for solid oxide cells, Prog. Mater. Sci. 133 (2023), 101050.

[52] F. He, Y. Zhou, T. Hu, Y. Xu, M. Hou, F. Zhu, D. Liu, H. Zhang, K. Xu, M. Liu, Y. Chen, An Efficient High-entropy Perovskite-type Air Electrode for Reversible Oxygen Reduction and Water Splitting in Protonic Ceramic Cells, Advanced Materials, n/a 2209469.